

Analysis of Ionosphere Gradient Using Japan GEONET Data

Hiroyuki Konno, Sam Pullen, Ming Luo, and Per Enge
Stanford University

ABSTRACT

Large spatial gradients in ionosphere delay are a potentially threatening error source for the Local Area Augmentation System (LAAS). Therefore a better understanding of the ionosphere behavior during strong magnetic storms is crucial for LAAS so that it can more accurately evaluate its integrity and availability during these events. In order to obtain spatially-dense information on severe ionosphere delays, we use data from the Japan GPS Earth Observation Network (GEONET). GEONET is a very dense network of dual-frequency GPS receivers with more than 1200 receivers distributed across Japan. This density provides a significant advantage to the investigation of local ionosphere behavior.

There are two major difficulties with the analysis of the GEONET data. The first issue is calculating accurate ionosphere delay measurements from the raw data provided by GEONET. We use the carrier-phase measurements of L1 and L2 while applying a calibration method for the interfrequency bias (IFB) that always appears in the processing of the dual-frequency data. The second issue is to screen out “artificial anomalies” that are due to GEONET receiver errors. Since the GEONET database is very large, partial data loss or erroneous measurements are occasionally included in the raw data. This poor-quality data can result in large errors in ionosphere delay calculations, and as a consequence, the estimated delays may appear to be ionosphere anomalies in the analysis. Based on identifying the geometrical differences between real and artificial gradients, we developed an error-screening technique that automatically excludes artificial gradients and output only actual large gradients from the huge GEONET database.

We investigated five strong magnetic storms using the GEONET data. We found several instances of ionosphere spatial gradients much larger than normal during these storms. However, we found no gradients extreme enough to lead to unacceptable user errors for LAAS. Through these analyses, we have demonstrated the effectiveness of our method as a tool to analyze ionosphere behavior based upon GEONET data.

1.0 INTRODUCTION

The Local Area Augmentation System (LAAS) provides real-time differential GPS corrections to aircraft users to support precision-approach operations. Since the service area of LAAS Ground Facility (LGF) is limited to the range of a user aircraft’s approach, the LGF and its user aircraft are close enough to cancel out the ionosphere delays in the user’s measurements with the DGPS corrections. However, if an LGF and/or user are exposed to a drastically large ionosphere gradient, the large difference of their ionosphere delays can result in a significant position error for the user. Therefore large spatial gradients in ionosphere delay are regarded as a potentially-threatening error source for LAAS.

Several examples of extremely large ionosphere gradients that could cause the significant user errors have been observed [1-4]. Datta-Barua et al. investigated the Wide Area Augmentation System (WAAS) “supertruth” data of April 6, 2000 and found an ionosphere gradient potentially as large as 316 mm/km [1]. Prior to this, the research that developed the ionosphere error model for LAAS estimated nominal ionosphere gradients at 3 ~ 5 mm/km (one-sigma) under active ionosphere conditions [5-6]. Therefore, the 316 mm/km gradient is more than 60 times the one-sigma nominal gradient. Triggered by this discovery, simulations for the purpose of quantitatively understanding the vulnerability of LAAS against the ionosphere anomalies have been conducted [7-9]. Luo et al. simulated the user position errors during hypothesized ionosphere anomalies based on an ionosphere gradient “threat space” model which explains the large ionosphere gradient with three parameters: slope of the ionosphere delay, width of the slope, and speed of the movement of the slope [8]. This work showed that anomalous gradients within the threat space model could create errors intolerable for LAAS and discussed the means to mitigate these cases by making them non-available in advance.

Although a better understanding about the vulnerability of LAAS against the ionosphere anomaly has been obtained from these simulations, an important question still remains open: do the threat models used in the simulations appropriately approximate real ionosphere spatial

anomalies? In order to evaluate the integrity of LAAS, the threat model must be conservative. However, if it is needlessly conservative, the evaluated availability will be unnecessarily low. Therefore, a model having appropriate and well-bounded parameters is crucial to achieving the maximum user benefits from LAAS. In order to obtain the best possible model, a good method for precisely analyzing actual ionosphere anomalies is needed.

In this paper, we introduce a method to analyze ionosphere anomalies by using the data from a very-dense network of GPS receivers in Japan, GEONET [10]. GEONET consists of more than 1200 dual-frequency receivers distributed throughout Japan. This degree of receiver density provides us with visibility of ionosphere delays to within 10 km to 50 km resolution, which is a significantly better than can be done with WAAS and IGS/CORS data from the U.S. In order to effectively deal with the huge GEONET database, we have employed a “coarse-to-fine” approach. First, we use a network of 350 ~ 400 receivers and search for ionosphere gradients larger than a particular threshold. In this process, receivers exposed to the gradients are identified. Next, we examine the data from all receivers located close to the identified receivers and fully analyze the ionosphere gradients affecting them.

In addition to sheer size, there are several difficulties in handling the GEONET data. The first difficulty is that, because only raw data is provided by GEONET, ionosphere delays must be calculated from this raw data. We use the carrier-phase measurements of L1 and L2 to calculate ionosphere delays. In general, combinations of dual frequency carrier-phase measurements provide us with less-noisy ionosphere delay. On the other hand, in order to calculate accurate delays, we need to calibrate the interfrequency biases (IFBs) of both receivers and satellites which come from hardware differences in the L1 and L2 signal paths. The IFB calibration problem is not a new problem in the GPS community, and several IFB-calibration methods have been proposed [11-13]. We apply one of these methods to the GEONET data, which is the method introduced by Hansen [11].

Another problem is the treatment of abnormal GEONET receiver behavior. Unfortunately, partial data loss and/or large receiver noise occur in the GEONET data on rare occasions. This poor-quality data results in large errors in the ionosphere delay calculation, and delays with large errors generally form large apparent gradients. In addition to this poor-quality data, imperfections in IFB calibration can cause ionosphere gradients to be significantly biased. These artificial gradients must be distinguished from real ionosphere anomalies. We have developed a noise-screening technique to do this which is based on the differing geometrical characteristics between artificially large gradients and actual large gradients.

We have analyzed five strong magnetic storms in Japan using the GEONET data. Based on the results of Luo’s simulations [8], we have concluded that no ionosphere gradient that could cause hazardous LAAS user errors occurred in these storms. Through these analyses, our method has demonstrated its effectiveness as a tool for analyzing the local-area ionosphere anomalies.

2.0 LARGE GRADIENT SEARCH ALGORITHM

In order to effectively handle the very large GEONET database, we developed a method based on a “coarse-to-fine” error analysis approach. In this section, we describe the algorithm for the “coarse” part. The objective of this algorithm is to search for ionosphere gradients larger than a threshold within the network of 350 ~ 400 receivers and identify the receivers exposed to the largest gradients. The main reason to use a subset of all GEONET receivers is to reduce the computation cost (processing time and memory limitations).

This algorithm consists of two processes: ionosphere gradient calculation and noise screening. In order to clearly describe the functions of these processes, we explain each process with showing results of a data processing for an actual strong magnetic storm occurred on November 6, 2001. This is one of the magnetic storms we have analyzed. The maximum Kp index of this storm is 8, and time at which the earth is impacted is estimated to be about 09:00 Japan Standard Time (GMT + 9 hours).

2.1 IONOSPHERE GRADIENT CALCULATION

Raw ionosphere delay estimates are calculated using the L1 and L2 carrier-phase measurements in GEONET data. As mentioned above, the primary difficulty of ionosphere delay calculation with dual-frequency data is dealing with the interfrequency bias (IFB) that appears in the model due to the combination of L1 and L2 measurements. The IFB is caused by hardware differences in the L1 and L2 signal paths and varies for each receiver and each satellite. For IFB calibration, we employed the method introduced by Hansen. The details of this method are presented in [11]. Here, we describe only the basics of the method.

The equations in (1) express the general form of the carrier-phase measurements on L1 and L2.

$$\begin{aligned}\phi_{L1} &= r + I + M_{L1} + N_{L1} \\ \phi_{L2} &= r + \gamma(I + IFB + Tgd) + M_{L2} + N_{L2}\end{aligned}\quad (1)$$

In these equations, r is the common term for the measurements of as range to a GPS satellite, receiver clock offsets, and troposphere delay. I is the ionosphere delay on the L1 signal. It is converted to the delay on the L2 signal by the multiplier γ , which equals the square of the L1 frequency (1575.42 MHz) divided by the square of the L2

frequency (1227.6 MHz). IFB is the interfrequency bias in the receiver RF path, and Tgd is the satellite RF path bias. M represents receiver multipath and thermal noise errors, and N is the integer ambiguity of the carrier-phase measurement.

The first step in utilizing these measurements for the calculation of the ionosphere delay is to estimate the integer ambiguities, N . In our method, the average of the differences of the pseudorange measurements and the carrier phase measurements over an entire satellite pass is assigned to be this ambiguity. Once this integer ambiguity estimation is done, the carrier-phase equations are combined to make the common term, r , vanish.

$$\begin{aligned} \frac{\hat{\phi}_{L2} - \hat{\phi}_{L1}}{\gamma - 1} &= I + \frac{\gamma}{\gamma - 1} (IFB + Tgd) \\ (\hat{\phi}_{L1} &= \phi_{L1} - N_{L1}, \quad \hat{\phi}_{L2} = \phi_{L2} - N_{L2}) \end{aligned} \quad (2)$$

Here M , the term representing multipath and thermal noise errors, is neglected, since this term is much smaller than the ionosphere delay (I) and IFBs (IFB and Tgd).

In order to solve this equation for the three unknown parameters I , IFB , and Tgd , Hansen constructed a linear equation, in which the ionosphere delay was modeled with spherical harmonics and Chapman functions. Spherical harmonics model the horizontal component of the ionosphere delay distribution in the solar geomagnetic coordinate system, and Chapman functions approximate the vertical component (the use of the geomagnetic frame is based on the fact that the ionosphere is less variable in this reference frame than in the earth-fixed frame). Applying these functions, equation (2) reduces to the following set of linear equations (shown in matrix form):

$$\frac{\hat{\phi}_{L2} - \hat{\phi}_{L1}}{\gamma - 1} = Ax \quad (3)$$

$A =$

$$\begin{bmatrix} A_{11} & \cdots & A_{1N} & | & \frac{\gamma}{\gamma-1} & 0 & \cdots & | & \frac{\gamma}{\gamma-1} & 0 & \cdots & 0 \\ A_{21} & \cdots & & | & \frac{\gamma}{\gamma-1} & 0 & \cdots & | & 0 & \frac{\gamma}{\gamma-1} & & 0 \\ \vdots & & & | & \vdots & & & | & \vdots & & & \\ A_{m1} & \cdots & A_{mN} & | & 0 & \cdots & \frac{\gamma}{\gamma-1} & | & 0 & 0 & \cdots & \frac{\gamma}{\gamma-1} \end{bmatrix}$$

$$x = [a_1 \quad \cdots \quad a_N \quad | \quad IFB_1 \quad \cdots \quad IFB_R \quad | \quad Tgd_1 \quad \cdots \quad Tgd_S]^T$$

The i^{th} row of this equation corresponds to the measurement of the i^{th} line of sight, LOS_i . The entry A_{ij} in the first part of the model matrix is an integral of j^{th} basis function of the

ionosphere model along LOS_i . The second part of the model matrix has non-zero entry, $\gamma/(\gamma-1)$, corresponding to the receiver from which this LOS_i begins, and the third part has the value of $\gamma/(\gamma-1)$ corresponding to the GPS satellite at the “end” of this LOS_i . The vector x is a state vector whose entries correspond to the coefficients of basis functions of the ionosphere model, the IFB of each receiver (IFB), and the IFB of each satellite (Tgd).

In our method, this set of linear equations is formed for each measurement update (every 30 seconds) and sequentially solved with a Kalman filter. Although the Kalman filter estimates the state vector at every epoch, the IFBs ($IFBs$ and $Tgds$) in the state vector estimated from the measurements at the last epoch are selected as the result of the IFB calculation (in other words, the Kalman filter solution for the last epoch in the data set is the one used to estimate the $IFBs$ and $Tgds$). Assuming each bias is constant for at least three days, we use data for three consecutive days to estimate one set of IFBs. Moreover, in order to reduce the random noise in the estimates, we take an average of IFBs that are estimated from three distinct data sets—the storm day itself, one week before the storm day, and one week after the storm day. Once reliable IFB estimates are obtained, ionosphere delays are obtained by subtracting the values of IFB and Tgd from each measurement.

The next step is the calculation of the spatial ionosphere gradients. Assigning each delay to its receiver’s position, we define the ionosphere gradient, G_{ij}^k , between two receivers (i and j) as follows:

$$G_{ij}^k = \frac{|I_i^k - I_j^k|}{d_{ij}}. \quad (4)$$

The superscript letter k represents the GPS satellite number, and d_{ij} is the distance between the two receivers. Since “local-scale” gradients are of more interest for this research than “wide-scale” gradients, we select the receiver pairs whose distances are between 30 km and 100 km.

Figure 1 is a three-dimensional histogram of the gradients obtained from the data of the magnetic storm that occurred on November 6, 2001. This histogram counts the number of gradients in bins that are divided with respect to gradient magnitudes and satellite elevation angles. Here, the elevation angle of a gradient is the average elevation of the two lines of sight that generate the gradient. Note that, in Figure 1, the z-axis shows the (base-10) logarithm of the number of occurrences. As can be seen, there exist remarkably large gradients, including multiple occurrences of gradients greater than 150 mm/km. According to the Luo’s simulation [8], the maximum gradient “tolerable” for LAAS is less than 80 mm/km in the vertical domain under

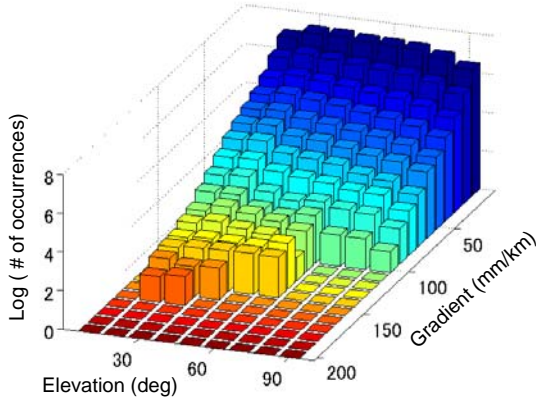


Figure 1: Histogram of slant gradients estimated by the ionosphere gradient calculation process

the conservative assumption that only 22 satellites are available and that the front of the ionosphere gradient stays between the user and LGF without moving (here, “tolerable” means that the vertical user error does not exceed 10 m). In order to compare our result with Luo’s simulation, the slant gradients must be transformed into vertical domain with 350-km thin-shell model [14]. Figure 2 is the resulting histogram of the vertical gradients. More than 1,400 intolerably large (*i.e.*, greater than 80 mm/km) gradients were detected in the November 6 data. However, inspecting these gradients, we noticed that some of these gradients were significantly inflated by errors in the ionosphere delay calculation. The existence of these artificially inflated gradients motivates the development of noise-screening processes described in the next section.

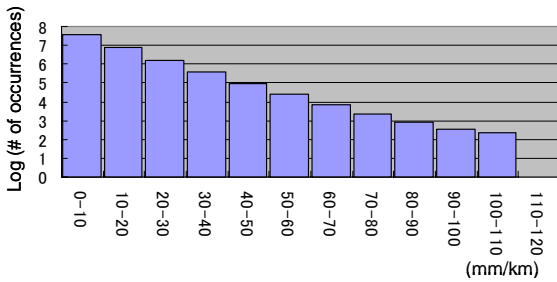


Figure 2: Histogram of vertical gradients

2.2 NOISE-SCREENING

The gradients estimated with the method described in the previous section incorporate the effect of random errors (E_{random}) and/or bias errors (E_{bias}) in the ionosphere delay calculation. Combining these error terms, the estimated

gradients are modeled as:

$$G_{ij}^k = G_{true} + E_{random}(I_i, I_j) + E_{bias}(I_i, I_j). \quad (5)$$

We are mainly interested in the gradients which cause large user errors for LAAS. Therefore gradients significantly inflated by calculation errors as to appear to threaten the LAAS users are a nuisance. Noise screening is a method that excludes such artificially inflated gradients. It comprises 3 processes: the Standard Deviation Test (SDT), Heuristic Rules, and Bias Error Exclusion (BEE). SDT is a technique to detect gradients inflated by large random noise. BEE, as the name implies, excludes gradients inflated by large bias errors. “Heuristic Rules” is a process that aggressively screens out “questionable” measurements based on information from the noisy measurements excluded by SDT.

Before starting the explanation of noise-screening processes, we need to define the term “large gradient”. “Large gradient” represents the gradients in which we are mainly interested from the point of view of possible hazards to LAAS users.

Large gradient =

$$\left\{ G_{ij}^k \left| \begin{array}{ll} G_{ij}^k > 80 \text{ mm/km} & \text{for elevation} > 60 \\ G_{ij}^k > 100 \text{ mm/km} & \text{otherwise} \end{array} \right. \right\} \quad (6)$$

The noise-screening processes were designed to exclude the artificially inflated gradients from the originally calculated set of large gradients. Only large gradients that pass through the noise-screening proceed to detailed analysis.

2.2.1 Standard Deviation Test (SDT)

Generally, large random noise in the ionosphere delay calculation results from faulty measurements. Because we use the data from hundreds of receivers, partial data breakage or large measurement errors do occur in the data sets on rare occasions. The resulting poor-quality data results in extremely large or small delays compared with neighboring delays that are calculated from correct measurements. In most cases, faulty measurements exist by themselves within a much larger network of valid measurements (faulty measurements are rare enough that multiple nearby faulty measurements are very improbable). Therefore ionosphere delays based on faulty measurements usually form “spike” errors.

Figure 3 shows an example of a spike error. Each bullet point indicates an ionosphere delay whose x and y components correspond to the receiver’s position and whose z component shows the amount of delay. As this figure implies, only one unusual delay estimate results in many large gradients because it is very different from all

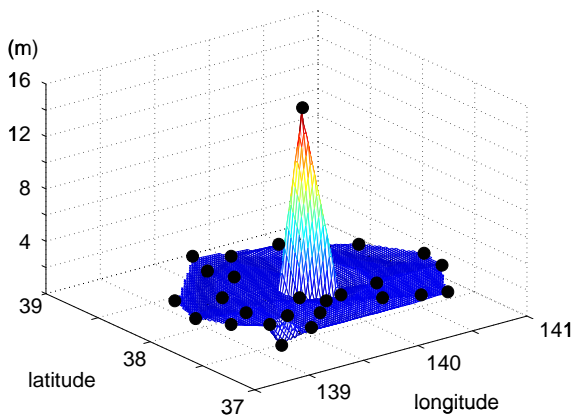


Figure 3: An example of a “spike error”

other delay estimates in its vicinity. In order to screen out this error, sampled standard deviations of the delays are calculated for each region in which a large gradient is observed, and delays with large residuals compared to this standard deviation are excluded. This process is called “Standard Deviation Test (SDT)” and is specified as follows:

- Select all delays which exist within 100 km from a large gradient.
- Calculate the standard deviation of these delays. Here, the largest and smallest delays in the selected delays are excluded from the calculation so that the calculated standard deviation will not be affected by these extreme values.
- All delays with residuals larger than 3σ are excluded from the original data.
- Apply the above three steps for all large gradients.

The radius within which data is compared (100 km) and the threshold for exclusion (3σ) are empirical parameters that were selected based on experience with GEONET data.

Figure 4 is the histogram of the ionosphere gradients for the November 6 data after applying SDT. About 36,000 faulty measurements were excluded by SDT. Of these, 2,455 were excluded from the set of apparent large gradients (this corresponds to just over 50 % of the original set of large gradients). About 2,400 large gradients remained after SDT.

2.2.2 Heuristic Rules

Inspecting the result of SDT led us to discover an interesting trend. As mentioned above, about 36,000 measurements were excluded with SDT; however, these

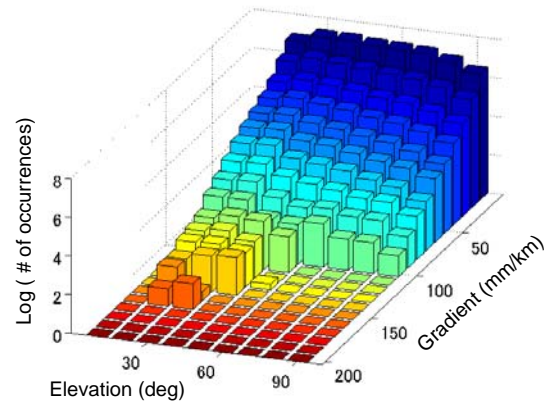


Figure 4: Histogram of slant gradients after applying SDT

measurements belonged to only 244 paths. This fact implies that the faulty measurements did not appear randomly but instead repeatedly appeared in particular paths. In addition, we noticed that paths with many faulty measurements tended to continuously yield large gradients even when their measurements were not regarded as faulty. Figure 5 illustrates this situation. Suppose measurements in portion A on the path are excluded with SDT (i.e., these measurements are faulty). The trend we found in the November 6 data is that, if portion A is relatively long, the measurements on the rest of the path (portion B) tend to generate large gradients with neighboring measurements.

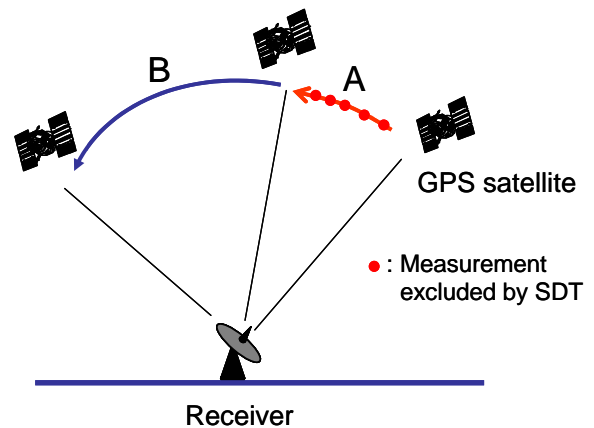


Figure 5: Illustration of a path that has many faulty measurements

Since GPS satellites move across the sky very fast, it is improbable that a particular path is continuously exposed to a large ionosphere gradient for such a long duration (large gradients do not move with a line of sight). Therefore

paths with large gradients over long duration can be regarded as “questionable”. The trend we found in the November 6 data indicates that the paths with many faulty measurements may be questionable from beginning to end (due most likely to ongoing problems with individual GEONET receivers).

Based on this analysis, we developed a rule to exclude such questionable paths:

- If a particular path has more than 30 measurements that are regarded as faulty by SDT, all measurements of this path are excluded (30 measurements corresponds to 15 minutes, since each measurement is updated every 30 seconds).

As with the SDT parameters, the threshold for exclusion (30 measurements, or 15 minutes) is an empirical parameter and is selected based on experience with the data.

In the November 6 data, we found that 98 receivers shared the 153 questionable paths, and 17 of these receivers had questionable paths on 3 or more satellites. As a rule of thumb, we regarded the receivers with more than 3 questionable paths as “questionable” and defined another noise-screening rule:

- If a receiver has more than 3 paths determined to be questionable paths by the previous rule, all measurements obtained by this receiver are excluded.

These two processes are named “Heuristic Rules”. These rules (especially the second one) may appear to be quite aggressive. It is possible for valid measurements to be excluded by these rules. However, if a measurement exposed to a real large-gradient event is screened out with the Heuristic Rules, this gradient would almost certainly be observed by neighboring receivers (due to the density of the GEONET network) and detected.

Figure 6 shows the gradient histogram for the November 6 data after applying both Heuristic Rules. An additional 1,763 large-gradients were newly regarded as faulty, and, as a consequence, only 634 large-gradients events remained.

2.2.3 Bias Error Exclusion (BEE)

The SDT algorithm described in Section 2.2.1 excludes gradients inflated by large random errors by searching for measurements that violate the expected spatial consistency of actual ionosphere delays. In this section, we introduce a separate method that screens out gradients inflated by the other error term in equation (3): bias errors in the ionosphere calculation.

In the discussion of Heuristic Rules in Section 2.2.2, we claimed that paths generating large gradients over long

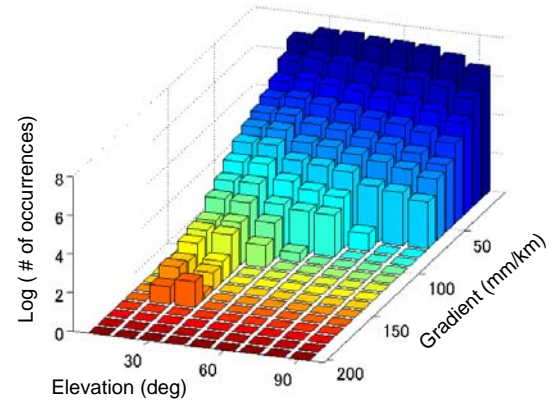


Figure 6: Histogram of slant gradients after applying Heuristic Rules

durations are almost certainly affected by some non-ionosphere-related error factor. Since this inflation appears in gradient estimates continuously rather than instantaneously, the error source is likely a hidden bias. Bias Error Exclusion (BEE) is a process that excludes such bias-inflated gradients by simply screening out gradients that continuously appear in the region of large gradients over a long duration as follows:

- If a particular gradient is continuously detected as a large gradient more than 120 times, which corresponds to 1 hour, all measurements that generate this gradient are excluded.

In contrast to SDT and Heuristic Rules, which designate the measurements yielding unnatural gradients, BEE excludes both of two measurements that generate unnatural gradients without specifying which of them is actually “biasing” the results. A drawback of BEE is therefore that there might be one valid measurement for each gradient excluded by BEE (of course, it is possible for both measurements to be simultaneously faulty). Considering this drawback, we selected a relatively large threshold, 120 times or 1 hour, so that BEE excludes only undoubted noise-inflated gradients. The cost of losing many valid GEONET measurements as a consequence was deemed acceptable.

Figure 7 is the gradient histogram for the November 6 data after applying BEE. BEE excluded 251 large gradients, leaving a total of 383 large gradients that passed through all stages of noise-screening. As can be seen in Figure 7, all of the large gradients are concentrated in the low-elevation region, as expected from slant gradient estimates. Transforming these slant gradients to the vertical gradients with the 350-km thin-shell model, we confirmed that no gradient that could threaten LAAS users (vertical gradients

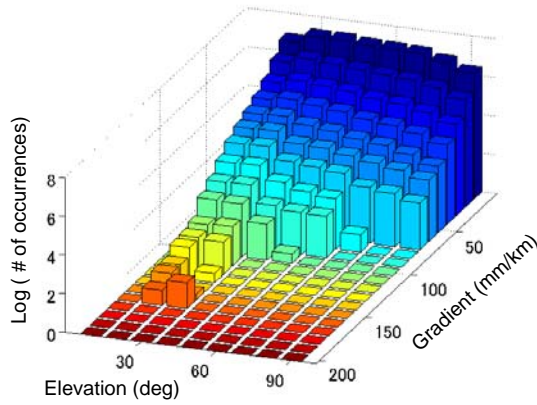


Figure 7: Histogram of slant gradients after applying BEE

larger than 80 mm/km) occurred in the November 6 storm. Figure 8 is a histogram of these vertical gradients.

In this section, we introduced the algorithm that searches for large ionosphere gradients within the GEONET database. In addition to the statistics of large gradients shown in this section, this algorithm provides us with knowledge of which receivers and satellites were exposed to large gradients and the times at which the large gradients affected them. Using this information, we can easily identify the data exposed to large gradients and conduct detailed analyses of the gradients using all (non-excluded) nearby GEONET receivers.

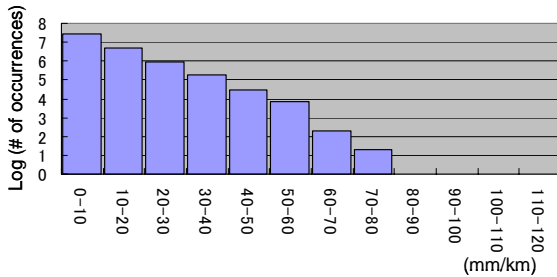


Figure 8: Histogram of vertical gradients after noise-screening

3.0 DETAILED ANALYSIS OF LARGE GRADIENTS IN NOVEMBER 6, 2001 DATA

In this section, we describe the detailed analysis of the large gradients found in the November 6, 2001 data. This analysis is an example of the “fine” component of our “coarse-to-fine” analysis method.

First, the time at which the large gradients occurred is

specified based on the information provided by the large-gradient search algorithm. Figure 9 shows the number of large gradients as a function of time. This plot shows that 16 large-gradients were detected at each epoch around 04:00 UTC. We recognized that 14 or 15 of these large gradients occurred on signals transmitted by PRN-21. We therefore focused on the ionosphere delays affecting measurements from PRN-21 in this study.

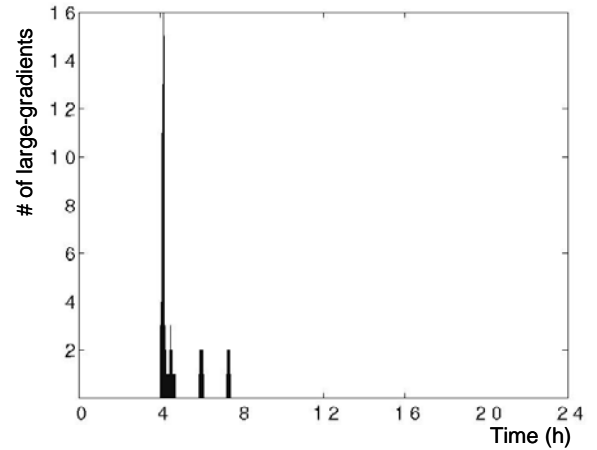


Figure 9: Number of large gradients as a function of time

We can view the overall ionosphere state by examining a distribution of vertical ionosphere delays. Figure 10 is a contour plot of vertical ionosphere delays at 04:06 (UTC), where each vertical delay is transformed from the slant delay with the 350-km thin-shell model and located at its notional 350-km-altitude pierce point. Small black dots indicate these pierce points, and each group of pierce points that forms the shape of Japan corresponds to the pierce points for the lines of sight that begin with a particular

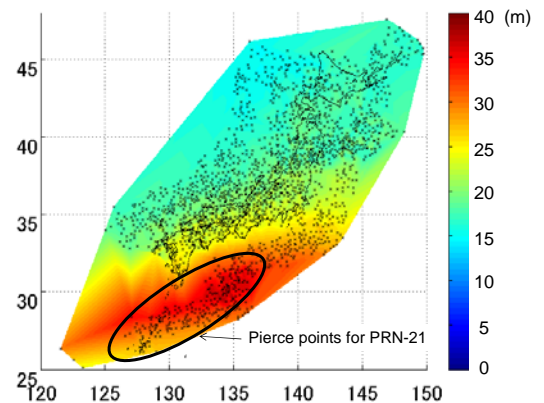


Figure 10: Contour plot of vertical ionosphere delay at 04:06(UTC)

satellite. The pierce points encircled in the ellipse are those for PRN-21. This plot shows that a region of large ionosphere delay exists south of Japan, and the peak vertical delay of this region is as large as 40 m. Moreover, the pierce points for PRN-21 are all located around this peak.

Based on this overall picture, we can proceed to examine the ionosphere delays for PRN-21. Figure 11 is a contour plot of the slant ionosphere delays for PRN-21 at 04:06 (UTC). In this plot, all slant delays are located at the observing GEONET receiver positions rather than at notional pierce points from the thin-shell model. Asterisks show the locations of the large gradients detected by the large-gradient search method. The white region over the northern part of Japan indicates that the receivers in this region had already lost the signal from PRN-21. This contour plot shows that the ionosphere delays increase from south to north roughly along meridians of longitude. This situation allows us to inspect the shape of these ionosphere gradients with the data of the receivers along a sample line of longitude.

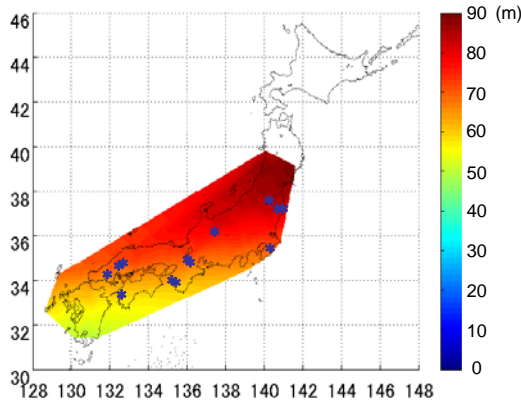


Figure 11: Contour plot of the slant ionosphere delay for PRN-21 at 04:06 (UTC)

We selected large gradients around 35° North and 136° East (see Figure 11) which are generated by RCV-639 and RCV-364 and by RCV-639 and RCV-312, and investigated the detailed configuration of the nearby ionosphere gradients. All receivers along 136° East were included in this investigation. Table 1 is the list of these receivers arranged in a north-to-south order. The column of “Distance” indicates the distance from that receiver to the next receiver in a southward direction.

Figure 12 shows the slant ionosphere delays at these receivers as they tracked PRN-21 over the part of its path visible to them. Each curve on the plot corresponds to the ionosphere delay at one receiver, and the order of the curves is the same the north-to-south order in Table 1. Ionosphere

Table 1: List of receivers along 136° East

No.	Receiver ID	Distance (km)	No.	Receiver ID	Distance (km)
1	RCV-259	13.4	6	RCV-364	30.0
2	RCV-580	26.4	7	RCV-312	35.6
3	RCV-056	31.7	8	RCV-824	20.0
4	RCV-320	26.0	9	RCV-367	33.2
5	RCV-639	57.5	10	RCV-316	-

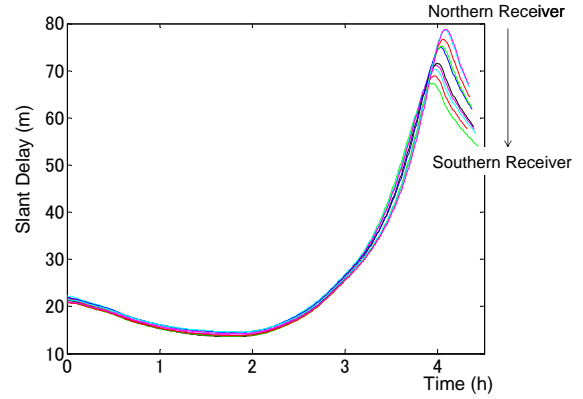


Figure 12: Slant delays of the sampled receivers through the entire path for PRN-21

delays are calculated with the method described in Section 2.1. Figure 13 shows the ionosphere gradients calculated from the ionosphere delays of two receivers adjacent to each other in Table 1. Each gradient, $G_i(t)$, is calculated from the following equation:

$$G_i(t) = \frac{I_i(t) - I_{i+1}(t)}{d}. \quad (7)$$

Here, i corresponds to the receiver number in Table 1 ($i = 1, 2, \dots, 9$), I_i is the ionosphere delay at receiver i , and d is the distance between the two receivers. Since the receivers in Table 1 are arranged in a north-to-south order, the gradients are positive when the northern receiver has a larger delay.

The high peak of the ionosphere delays in Figure 12 corresponds to the lines of sight of the receivers passing through the large ionosphere delay region south of Japan as shown in Figure 10. As these lines of sight pass through this region, the ionosphere gradients rise steeply (see Figure 13). Two of the gradients finally exceed 100 mm/km. These gradients are generated by RCV-580 and RCV-58 (the red curve) and by RCV-639 and RCV-364 (the green curve). The gradient by RCV-639 and RCV-364 was detected with the large-gradients search method. The other was not, because RCV-58 was not used in the large-gradient search method. As noted in Section 1.0,

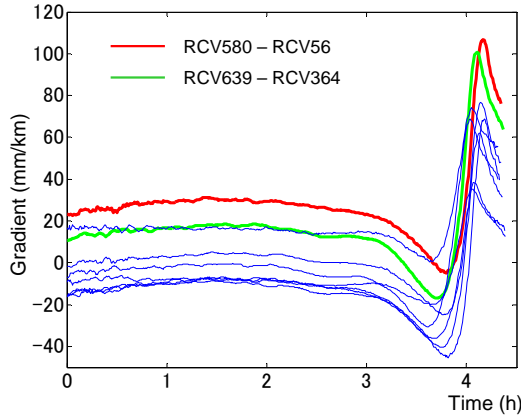


Figure 13: Gradient vs Time

only about 30% of all GEONET receivers could be used in the search method due to processing time and memory limitations. Despite this, once a severe gradient is identified by the search method, all nearby GEONET receivers can be used to better characterize it.

It also can be seen in Figure 13 that most gradients have biases relative to each other. In particular, these errors are clearly seen in the region where all gradients are relatively flat (from about 01:00 to 03:00). The residual errors of the IFB calibration are the probable cause of these errors. In order to exclude the effect of these bias errors, we arbitrarily made all gradients equal to 0 at 01:00. In other words, we assumed that all ionosphere delays have the same value at 01:00. Since this “leveling” was done at 01:00, it occurred well before the gradient transition period. Figure 14 shows the gradients after this modification. The red curve and green curve in Figure 14 correspond with those in Figure 13. In Figure 14, all gradient curves become almost identical during the flat period, and the maximum gradient during the active (“sloping”) period around 04:00 is reduced to 83 mm/km.

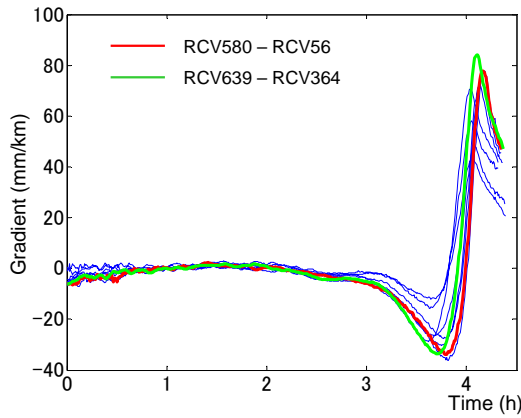


Figure 14: Modified Gradients vs Time

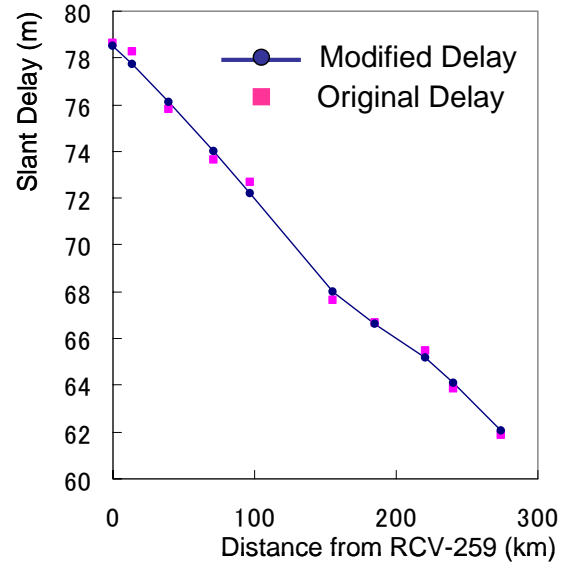


Figure 15: Distribution of the ionosphere delays at the selected receivers at 04:06 (UTC)

Finally, Figure 15 shows the ionosphere delay distribution at 04:06, when the ionosphere gradient reached its largest value. Blue bullets indicate ionosphere delays at each receiver after “leveling” modification, and red bullets indicate the original values. The x-axis shows the distance of each receiver from RCV-259 (the northern most receiver). This figure shows that the ionosphere delay distribution is visualized with high resolution. In addition, we notice that the modifications of the delay values are quite small. This suggests that the analysis of the ionosphere gradient is very sensitive to the bias error in the ionosphere delay calculation. This results from the fact that we are describing the gradients in the range of mm/km and that the distance between two adjacent receivers (the denominator of equation (7)) is small. However, we believe that, if the ionosphere gradient is 100 mm/km or more (the critical level for LAAS), the bias error will not be a serious problem for the analysis.

In this section, we have described an example of the detailed analyses performed on the large gradients detected with the large-gradient search algorithm. The result of this analysis demonstrated that the GEONET data allows us to visualize the detailed configuration of ionosphere delays around large gradients with high resolution. On the other hand, we also recognize that the quantitative result could be ambiguous due to the bias errors in the ionosphere delays. This bias problem should be treated on a case-by-case basis. However, the very dense GEONET data provides the ionosphere delay information at multiple points in the region of interest and is sufficient to distinguish gradients threatening to LAAS from anomalous but smaller gradients.

4.0 SUMMARY OF OTHER MAGNETIC STORMS

In addition to the November 6, 2001 magnetic storm, we have analyzed four other strong magnetic storms. We selected these storms based on the maximum Kp index and the estimated time at which they hit the Earth. The storms that are estimated to have impacted the Earth during Japanese local daytime were selected, with the exception of the storms on October 29, 2003 and November 20, 2003. Extremely large ionosphere gradients were observed from GPS data obtained in the United States on October 29, 2003 [3-4] and November 20, 2003 [4]. We therefore include these days to see if some large gradients were also observed in the GEONET data. Table 2 lists of these storms.

Figure 16 shows histograms of the ionosphere gradients for these storms. These histograms show the situations after the noise-screening steps of the large-gradient search algorithm. As can be seen in this figure, some large gradients are detected, especially in the low-elevation region. However, having referred to the simulation results

Table 2: List of strong magnetic storms analyzed in this work

Date	Estimated time of impact on the Earth	Max Kp
Mar. 31, 2001	00:23 (9:23 JST)	9
Nov. 6, 2001	00:09 (9:09 JST)	8
Nov. 24, 2001	05:00 (14:00 JST)	9
Oct. 29, 2003	18:00 (Oct. 30 3:00 JST)	9
Nov. 20, 2003	08:04 (17:04 JST)	9

in Luo [8], we concluded that there were no ionosphere gradients large enough to be critical for LAAS users above Japan during these storms. In particular, it is interesting that no large gradient was detected within the October 29, 2003 and November 20, 2003 data. We believe that this because the ionosphere behavior that resulted in the significant gradients in the United States had already “calmed down” when Japan passed under the affected region of the ionosphere.

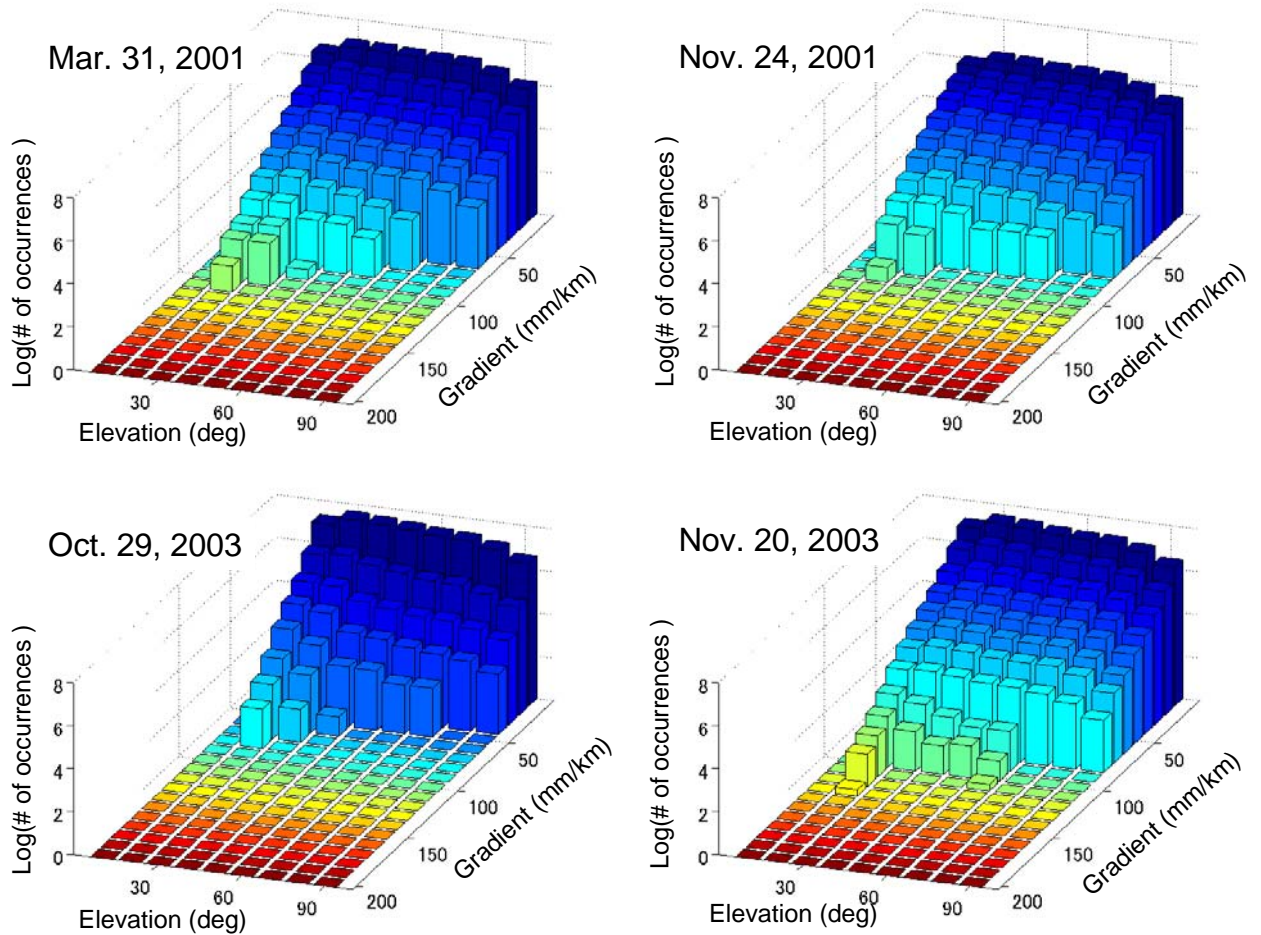


Figure 16: Histograms of slant gradients for magnetic storms analyzed in this work (after noise-screening)

5.0 CONCLUSION

In this paper, we introduced a method to analyze ionosphere anomalies using Japan GEONET receiver data. The density of the GEONET receiver network is a significant benefit to the analysis of small-scale ionosphere behavior. On the other hand, errors within the GEONET data and the imperfections of the ionosphere delay calculation result in “artificial anomalies” as well as “real” ones. The large-gradient search algorithm screens out these errors and detects data that are exposed to real large gradients. Once the time, location, and affected receivers are specified, the density of the GEONET data provides us with high-resolution visibility of the ionosphere distribution around the gradients. The analysis described in Section 3 demonstrated the potential of this process based on GEONET data.

While we have found several instances of anomalously-large ionosphere gradients near Japan, particularly in the regions south of Japan that are affected by equatorial ionosphere anomalies, we have not found any evidence of gradients large enough to threaten LAAS users. This may well be a good news for research into a Japanese Ground Base Augmentation System [15-16]. However, there is no guarantee that such ionosphere gradients will never happen. Continuing to search for large ionosphere gradients within GEONET data is therefore an important task for the future.

In this paper, we focused only on the slope of the ionosphere delays. Based on the simulations in [8], it is apparent that the speed of motion of ionosphere gradients relative to a fixed LAAS site is also an important parameter for evaluating the potential impact on LAAS. The density of the GEONET data will make it easier for us to evaluate the movement of the ionosphere gradients in Japan compared to the less-dense data available for the U.S.

The primary characteristic of our method is using a quite unique data source, GEONET. However, the large-gradient search algorithm described in Section 2 can be applied to other data sources, such as WAAS and IGS/CORS. Applying our method to other data sources is also an interesting task for the future. Since the Standard Deviation Test (Section 2.2.1) requires a certain degree of receiver density, this task will not be simple. However, if we can adequately apply this concept to other data sources, it must be a powerful tool for analyzing them.

In addition to the assessment of the ionosphere behavior, we can simulate LAAS performance using GEONET data, assuming one receiver to represent an LGF and neighboring receivers to represent users. This is a simulation of ionosphere gradient impact based upon actual GPS data, and we can use this concept to obtain a better understanding about the real-world performance of LAAS against ionosphere anomalies.

ACKNOWLEDGMENTS

We gratefully acknowledge the support from FAA LAAS Program Office (AND-710) in funding this research. We would also like to thank Takeyasu Sakai at Electronic Navigation Research Institute for providing us with the software for IFB calibration. We would also like to thank Geographical Survey Institute of Japan for providing us with GEONET data.

REFERENCES

- [1] S. Datta-Barua, *et al.*, "Using WAAS Ionospheric Data to Estimate LAAS Short Baseline Gradients," *Proceedings of the ION 2002 NTM*, Anaheim, CA., Jan., 2002, pp. 523-530.
- [2] T. Walter, *et al.*, "The Effects of Large Ionospheric Gradients on Single Frequency Airborne Smoothing Filters for WAAS and LAAS," *Proceedings of ION 2004 Annual Meeting*, San Diego, CA., Jan., 2004.
- [3] A. Komjathy, *et al.*, "The Ionospheric Impact of the October 2003 Storm Event on WAAS," *Proceedings of ION GNSS 2004*, Long Beach, CA., Sept., 2004, pp. 1298-1307.
- [4] T. Dehel, *et al.*, "Satellite Navigation vs. the Ionosphere: Where Are We, and Where Are We Going?," *Proceedings of ION GNSS 2004*, Long Beach, CA., Sept., 2004, pp. 375-386.
- [5] G. McGraw, *et al.*, "Development of the LAAS Accuracy Models," *Proceedings of ION GPS 2000*, Salt Lake City, UT., Sept., 2000, pp. 1-12.
- [6] S. Pullen, "Summary of Ionosphere Impact on PT 1 LAAS: Performance and Mitigation Options," Stanford University, Dept. of Aeronautics and Astronautics, Dec. 14, 2000.
- [7] M. Luo, *et al.*, "LAAS Ionosphere Spatial Gradient Threat Model and Impact of LGF and Airborne Monitoring," *Proceedings of ION GPS 2003*, Portland, OR., Sept., 2003.
- [8] M. Luo, *et al.*, "Ionosphere Spatial Gradient Threat for LAAS: Mitigation and Tolerable Threat Space," *Proceedings of ION 2004 Annual Meeting*, San Diego, CA., Jan., 2004.
- [9] M. Luo, *et al.*, "Ionosphere Threat to LAAS: Update Model, User Impact, and Mitigations," *Proceedings of ION GNSS 2004*, Long Beach, CA., Sept., 2004, pp. 2771-2785.
- [10] Homepage of Geographical Survey Institute of Japan http://terras.gsi.go.jp/inet_NEW/

[11] A. Hansen, "Tomographic Estimation of the Ionosphere Using Terrestrial GPS Sensors," *Ph.D Dissertation*, Stanford University, Dept. of Aeronautics and Astronautics, Mar. 2002.

[12] B. Wilson, *et al.*, "New and Improved The Broadcast Interfrequency Biases," *GPS WORLD* Sept., 1999, pp. 56-66.

[13] P. Camargo, *et al.*, "Application of ionospheric corrections in the equatorial region for L1 GPS users," *Earth Planets Space*, 52, 2000, pp.1083-1089.

[14] P. Misra, P. Enge, *Global Positioning System: Signals, Measurements, and Performance*. Ganga-Jamuna Press, 2001.

[15] S. Saitoh, *et al.*, "Experimental GBAS Performance at the Approach Phase," *Proceedings of the ION 2003 NTM*, Anaheim, CA., Jan., 2003.

[16] T. Yoshihara, *et al.*, "A study of the ionospheric effect on GBAS (Ground-Based Augmentation System) using the nation-wide GPS network data in Japan," *Proceedings of the ION 2004 NTM*, San Diego, CA., Jan., 2004.